TECHNICAL ARTICLE

Micromechanical Analysis of Metal-Ceramic Thin-Films on Steel Substrates

R. CHEN [1,3] N. GRIGOREV,[2] R. SCHWAIGER [1]
and S. BRINCKMANN [1,4]

1.—Institute of Energy and Climate Research, IEK-2: Structure and Function of Materials, Forschungszentrum Jülich GmbH, 52425 Jülich, Germany. 2.—Institute of Mineral Engineering, RWTH Aachen University, 52062 Aachen, Germany. 3.—e-mail: ru.chen@fz-juelich.de. 4.—e-mail: s.brinckmann@fz-juelich.de

Thin-layered coatings on material surfaces can resist contact forces and provide protection against material wear. In this study, FeCrNi-Al_2O_3 composite coatings were prepared by electrodeposition onto a 316L steel substrate. The effects of electrodeposition cathode current density (3 A·dm^{-2}, 5 A·dm^{-2}, 7 A·dm^{-2} and 9 A·dm^{-2}) and post annealing at 500°C in Ar atmosphere were investigated. An increase in deposition rate resulted in a rougher coating surface and a thicker coating at a constant deposition duration. Post-deposition heat treatment caused the surface roughness to increase because of the introduction of denser micro-cracks. Higher current densities improved adhesion and prevented angled cracks during scratching, while annealing led to scratching-induced failures at lower applied loads. FeCrNi-Al_2O_3 composite coatings showed higher hardness but lower Young's modulus compared to the steel substrate. The coating hardness is slightly enhanced by increasing the electrodeposition current density from 5 A·dm^{-2} to 9 A·dm^{-2}, and a more significant increase is observed after annealing. However, the hardness is negatively impacted by the combined effect of annealing and higher current density. These findings demonstrate the importance of carefully balancing the electrodeposition current density and annealing conditions to achieve optimal coating properties. To optimize metal-ceramic composite coatings, it is crucial to investigate multiple process parameters that may interact with each other.

INTRODUCTION

Modern coatings are used to modify the surfaces of technical components and significantly enhance their performance, making them indispensable in numerous industrial sectors.[1] The chemical composition and process parameters of the coating material need to be adjusted to provide adequate protection of substrates against scratches, wear and corrosion. Moreover, coatings are applied to effectively enhance solderability, lubricity, electrical conductance, corrosion resistance and wear resistance of the substrate materials.[2,3] One of the most versatile fabrication processes to produce coatings is electrodeposition, which makes thin films of metals and alloys with well-defined chemical and mechanical properties.[4]

Among various coating types, metal-matrix composite coatings have received considerable attention in both research and practical applications.[5,6] In general, Fe-based alloys are preferred for surface modification of steel parts because of their similar composition and excellent performance. In addition, their affordability makes them attractive for commercial applications. To further improve the microstructural and mechanical properties of Fe-based alloy coating, the incorporation of other metals has been explored to form binary or quaternary alloys, such as Ni-Fe,[5] Fe-Mn,[7] Fe-Co-Ni[8] and Fe-Cr-Ni.[9] In particular, FeCrNi alloy coatings produced by electrodeposition have attracted much attention because of their excellent corrosion

resistance and mechanical properties.[10–12] They are, for example, promising candidates for advanced biomedical systems as shown in a study of amorphous FeCrNi thin films with varying Cr contents.[11] This is due to their unique combination of superior corrosion resistance, low cytotoxicity and soft magnetic properties.

Composite coatings are increasingly replacing conventional coatings in many commercial applications.[13,14] In particular, the addition of ceramic particles has been considered because of their high hardness, good wear and corrosion resistance compared to metal coatings.[15–17] The presence of ceramic particles in the coating can improve the tribological properties and corrosion resistance of the coating by forming a chemical bond with the matrix material.[18] Starosta et al.[19] investigated a NiFe-Al_2O_3 composite coating and found that Al_2O_3 improved the wear resistance, which depended on the particle size and density. In addition, Al_2O_3 particles embedded in Ni-based coatings were reported to increase corrosion resistance by improving the microstructure of the coatings.[20] However, it remains a challenge to control the uniform dispersion of ceramic particles in the metal-matrix coating. The inhomogeneous distribution of ceramic particles in the metal matrix can lead to pores in the coating, which adversely affects the mechanical performance.[21] In addition, there is a mismatch between the elastic properties of the ceramic and the metal, which leads to increased interfacial stresses and interfacial cracking.[22] To solve these problems, suitable processing methods must be developed.

In this study, we investigated the microstructure and mechanical properties of composite coatings consisting of FeCrNi and with embedded Al_2O_3 nanoparticles. The influence of the applied current density of the electrodeposition process on the micromechanical properties of such composite coatings on 316L steel substrates was studied. To understand the effect of residual stresses generated during the manufacturing process, the changes in the coating morphology and the mechanical properties after annealing at 500°C in an Ar atmosphere were investigated. Micromechanical analysis was performed by scratch and depth-sensing indentation tests comparing scratch resistance, microhardness and deformation behaviors.

MATERIALS AND METHODS

Specimen Preparation

In this study, FeCrNi-Al_2O_3 composite coatings were prepared by electrodeposition on a 316L steel substrate. In the first step, chromium (III) chloride hexahydrate and glycine were dissolved in distilled water. The solution was then heated to 80°C and kept at this temperature for 30 min. The resulting solution was cooled to room temperature and continuously stirred for the next 12 h. In the second step, the remaining chemicals from Table I were dissolved in distilled water in a separate beaker.

Table I. Electrodeposition parameters for FeCrNi-Al_2O_3 composite coating

Electrodeposition parameters	Value
Electrolyte composition	
$CrCl_3·6H2$ O (≥ 98%, Sigma-Aldrich)	106.56
H_2NCH_2COOH (≥ 99%, Sigma-Aldrich)	30.03
$FeCl_2·4H_2O$ (98%, Sigma-Aldrich)	5.97
$NiCl_2·6H_2O$ (VWR chemicals)	47.54
NH_4Cl (Merck KGaA)	2.75
H_3BO_3 (min. 99.5%, Alfa Aesar)	9.28
NaCl (min. 99%, Th. Geyer GmbH&Co. KG)	29.22
Current density (A·dm-2)	3, 5, 7, 9
Coating time (min)	90
Temperature (°C)	23
Anode-cathode distance (mm)	20
Bath stirring (rpm)	200

Both solutions were mixed in a volume ratio of 1:1. Then, in a proportion of 30% of the final volume, ethylene glycol was added. The pH of the solution was adjusted to 1 by adding 1 M hydrochloric acid.

To produce the composite coatings, Al_2O_3 particles (Sigma-Aldrich alumina nanopowder, 1 g/L, particle size < 50 nm) were added to the electrolyte. Before starting the experiment, the suspension was ultrasonically dispersed for 5 min. In addition, the solution was sonicated every 15 min for 1 min during the coating process to avoid possible agglomeration as well as sedimentation of the powder. A nickel sheet (MARAWE GmbH & Co. KG) was used as anode. Electrodeposition was carried out at a current density of 3 to 9 A·dm^{-2}. Further deposition parameters are listed in Table I. In addition, the effect of thermal annealing was investigated. After electrodeposition, four samples deposited at different current densities were subjected to heat treatment at 500°C for 1 h in an Ar atmosphere.

Scratch Test

Scratch tests were performed using a Rockwell diamond indenter in a CSM nano- and microindenter (CSM instruments SA, now Anton Paar GmbH, Ostfildern, Germany). A progressive load (0.03–20 N) was applied over a scratch length of 2 mm during each test. The load rate was 9.98 N/min and the scratch speed 1 mm/min. When the applied load is increased progressively, a scratch mark with increasing width is formed, which leads to failure in the form of cracking, delamination, fragmentation and chipping. During the scratching, the tangential force F_T, penetration depth P_d, R_d and acoustic emission Ae signals were recorded with the increase of normal force F_N. A plot of a typical scratch experiment is shown in Fig. 1a. Before and after the progressive scratching, the surface was scanned along the scratch direction with a constant load of 0.03 N, as schematically shown in Fig. 1b.

The ratio between tangential and normal force represents the apparent coefficient of friction (COF,
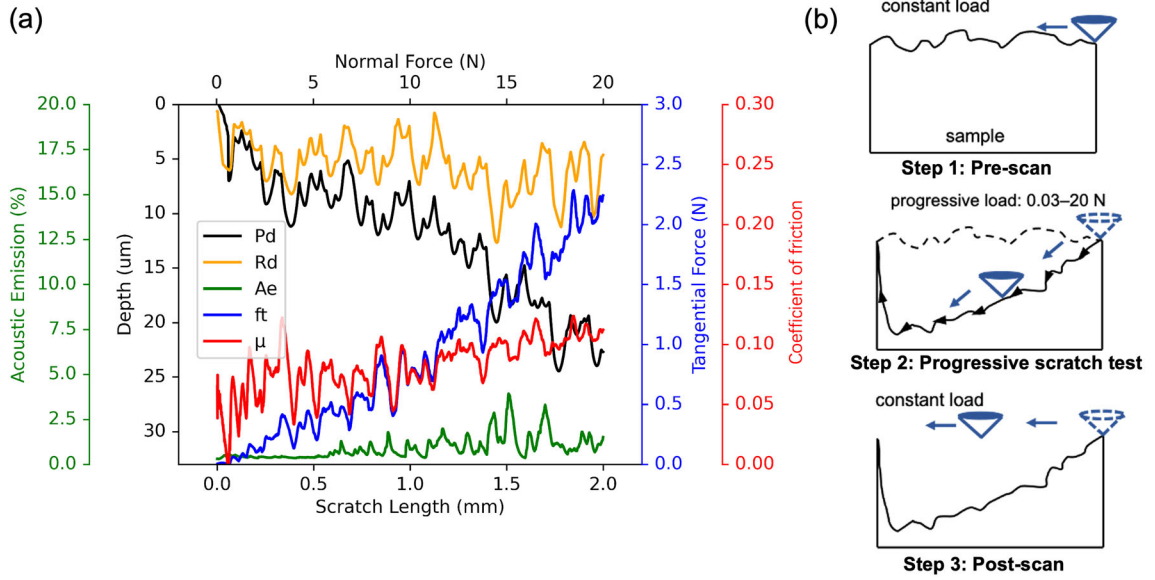
Fig. 1. (a) Data acquired during a typical scratch test with a progressive normal force. The instantaneous depth P_d and the residual depth R_d are shown on the left-hand y-axis as well as the acoustic emission signal. The tangential force F_t and the friction coefficient COF are shown in blue and red, respectively. With the increase of the force, the indenter penetrated deeper in the sample. (b) Schematic showing the three steps of a scratch test consisting of a pre-scan (here, at 0.03 N), the progressive scratch test (ramping the load from 0.03 N to 20 N) and a post-scan (at 0.03 N) (Color figure online).

Eq. 1), which is used to analyze deformation and damage of surfaces under tribological loading.[23]

$$\text{COF} = \frac{F_t}{F_N} \quad (1)$$

The acoustic emission and the tangential force signals can be used to identify characteristic events, such as crack nucleation and delamination. However, we did not observe a correlation of the acoustic emission peaks with failure events in this study and will therefore not consider acoustic emission in the further discussion.

Each scratch test consists of three strokes, i.e., the pre-scan profile, the scratching at a progressive normal load, and the post-scan profile (Fig. 1b). The pre-scan profiling takes surface roughness and topography into account, while the instantaneous penetration depth P_d is determined during scratching. P_d is calculated as the difference between the depth of the pre-scan profile d_{pre} and the penetration depth d_p (Eq. 2). The post-scan profiling provides the residual depth d_{post} to evaluate the residual deformation. The difference between the pre- and post-scan depths determines the residual scratch depth R_d (Eq. 3).

$$P_d = d_p - d_{pre} \quad (2)$$

$$R_d = d_{post} - d_{pre} \quad (3)$$

The difference between the penetration depth and the residual depth reflects the elastic deformation of the material during the scratch test. This elastic deformation is recovered after the removal of the

indenter. The ratio between the elastic deformation and the total deformation is termed elastic recovery ratio ERR (Eq. 4) and reflects the resistance of the coating to permanent deformation:[24]

$$\text{ERR} = \frac{P_d - R_d}{P_d} \quad (4)$$

The normal force that results in a certain coating failure is referred to as the critical scratch load for a particular failure type. In this study, we are considering three failure types and their corresponding critical forces:

• The formation of cohesive cracks inside the coating, where L_{C1} is the force responsible for the first occurrence of cohesive cracks,
• Discontinuous delamination of the coating from the substrate, which occurs because of forces of at least L_{C2},
• Forces equal to or greater than L_{C3} led to the continuous delamination of the coating from the substrate.

Depth-Sensing Indentation

Indentation was performed on all coated samples as well as on the uncoated 316L stainless steel substrate using a Berkovich tip, whose area function was calibrated using measurements in fused silica. The measurements were conducted using an MTS NanoIndenter XP (MTS Systems Corp., Eden Prairie, MN, USA), which is a force-controlled device, with the continuous stiffness measurement (CSM) option and were analyzed following the

Oliver and Pharr method.[25] The CSM option allows the continuous measurement of mechanical properties along the loading curve, allowing to monitor hardness and stiffness already at the early stages of the indentation process. Prior to the indentation test, all samples were mechanically polished with diamond suspensions to reduce the effect of surface roughness on the indentation results. The samples were then indented at a constant strain rate (constant (dP/dt)/P) of 0.05 s^{-1} to a depth of 2000 nm. At the maximum depth, a dwell time of 10 s was specified. Finally, the samples were unloaded to 10% of the maximum load and the load was held constant for 20 s to evaluate the thermal drift during the measurements. Twelve indents were performed on each sample.

Microscopic Investigation

The surface morphology of the coating was studied by scanning electron microscopy (SEM, Zeiss Merlin, Carl Zeiss Microscopy GmbH, Oberkochen, Germany). The chemical composition for selected regions of samples was analyzed using energy-dispersive X-ray spectrometry (EDS, Oxford Instruments GmbH, Wiesbaden, Germany).

An Olympus OLS4000 3D confocal laser scanning microscope (CLSM) was used to locate, image, and examine the scratch tracks and associated surface damage. The thickness of the coating was measured on cross sections of the FeCrNi-coated samples using the same microscope. CLSM images were further analyzed using the *Gwyddion* software[26] to analyze surface roughness as well as microstructural damage along the scratch tracks. To image the entire scratch track from start to finish, nine individual images were stitched together.

RESULTS AND DISCUSSION

Morphology of the Coatings

The morphology of FeCrNi-Al$_2$O$_3$ composite coatings varies with the current density of electrodeposition and the heat treatment. Coating thickness and surface roughness are summarized in Table II. The coating thickness increased from 4.2 μm at 3 A·dm^{-2} to 20.4 μm at 9 A·dm^{-2} for the same electrodeposition time, while it was not affected by the heat treatment after fabrication. Theoretically, the amounts of dissolved anode and deposited metal ions are directly dependent on the magnitude of the current density. According to Faraday's law,[27] the theoretical deposition rate would increase linearly with the current density. As the current density increases, the cathode exerts a strong electrostatic attraction, causing the cathode potential and polarization to increase steadily. Therefore, the increased coating thickness at the cathode was expected at higher current densities.

Comparing the cross sections of the as-deposited and annealed samples by SEM (Fig. 2) shows that the Al$_2$O$_3$ distribution has changed after annealing at 500°C. Nano-sized Al$_2$O$_3$ particles accumulated at the bottom of each coating layer in the as-deposited samples. The Al$_2$O$_3$ particle distribution is also evident from the chemical elements analysis by EDS, as shown in Fig. 2e, f, g, h, i, and j. In annealed samples, these ceramic particles appear to be distributed more homogeneously. Additionally, the particle distribution is also influenced by the small variations in deposition rate at different parts of the sample during production. The inhomogeneous distribution of ceramic particles in the metal matrix can lead to pores in the coating, which is detrimental to the mechanical performance.[21] However, the particle distribution and elemental composition measured from just one specific polished surface may not represent the entire coating.

The surface roughness of the coating increases with increasing current density and increases further after annealing (Table II). The higher surface roughness may promote various undesirable tribological phenomena such as wear and fatigue. The change of roughness is evident in the CLSM images showing the surface appearance of the samples produced by different deposition current densities and heat treatment (Fig. 3).

As the current density increases, the surface becomes rougher and exhibits a cauliflower-like morphology; more bumps and nodules are observed on the surface. The faster the growth rate at higher current densities, the higher the consumption rate of metal ions near the cathode surface compared to its replenishment rate. Thus, mass transfer dominates the electrodeposition and concentration polarization occurs. This polarization leads to a nodular structure resulting from the uncontrolled growth of the coating protrusions and increase in the coating roughness.[28] On the one hand, the ceramic alumina particles can act as nucleation sites and promote the formation of nodules with a larger size variation.[29] On the other hand, the Al$_2$O$_3$ phase has a low conductivity such that the reduction of metal ions becomes more difficult and the electrodeposition process slows down in areas of high alumina content.[19] Hence, the deposition rate varies in different areas because of the distribution of Al$_2$O$_3$ particles, which influence the surface roughness.

The surface after annealing is covered with microcracks, indicating either an increase in the residual stresses of the coating layers or embrittlement due to the heat treatment. At higher current density, the surface became rougher as measured in annealed samples (Table II), while more cracks were observed on the surface (Fig. 3). For coatings that are thicker because the current density was higher, residual stresses would also be higher than for thinner coatings, in particular the residual stresses caused by the thermal expansion mismatch between coating and substrate. Cracking is a problem in the electrodeposition of Cr-based alloy coatings, mostly related to the decomposition of

Table II. Coating thickness and surface roughness of the coatings

Sample			
Current density (A·dm^{-2})	Heat treatment	Coating thickness (μm)	Arithmetical mean roughness (R_a) (μm)
3	As-deposited	4.24 ± 0.42	1.41
	Annealed	4.76 ± 0.23	1.72
5	As-deposited	12.71 ± 0.24	1.62
	Annealed	12.53 ± 0.18	2.21
7	As-deposited	16.44 ± 0.38	1.73
	Annealed	16.21 ± 0.62	2.41
9	As-deposited	20.48 ± 0.64	2.07
	Annealed	21.65 ± 0.41	4.15

unstable Cr hydride (CrH_x).[12] The hydrides are easily decomposed from a hexagonal structure to body-centered cubic metallic Cr, resulting in volume shrinkage and thus crack formation. High temperature treatment would promote the transition of hydrides into metallic Cr, which increases crack growth and widens the cracks. A similar fracture phenomenon in FeCrNi alloy coatings was reported by Bertero et al.,[12] cracking and decomposition of hydrides as well as an increasingly chromium oxides and carbides during annealing were identified as the main cause. In addition, the cracks in the coatings are enlarged by the oxidation of the coating resulting in an oxide that has a lower fracture toughness than its metallic counterpart. During annealing, the surface tends to be oxidized as revealed by EDS analysis in the present study (Fig. 4). These oxides were composed mainly of chromium and iron oxides. The cracks did not penetrate the whole coating or expose the substrate, which we confirmed by EDS inside the crack and the lack of Mn, which is contained in the steel substrate.

Scratch Behavior

As exemplified in Fig. 1, the penetration depth increased during scratching with progressive load. For all samples, the scratch tests resulted in a final penetration depth exceeding the coating thickness. As shown in Fig. 5a, the penetration depth increased with increasing current density and coating thickness. The samples deposited at a current density of 3 A·dm^{-2} exhibit the smallest penetration depths. Since annealing did not change the coating thickness as discussed above, the penetration depth of as-deposited and annealed samples is comparable. In addition, the change in current density and heat treatment had little influence on ERR (Fig. 5b). The smaller penetration depths suggest a harder coating and better resistance to scratch deformation, while a higher ERR (see Eq. 3) indicates superior resistance to permanent deformation.

The COF as a function of scratch length, which increases with increasing F_N, is plotted for coatings without and with annealing in Fig. 5c and d, respectively. The measured COF can be expressed as the sum of plowing and adhesive friction.[24] In all samples, the increase of COF can be observed at higher applied load. Compared with samples deposited at 3 A·dm^{-2} current density, the COF exhibits significant fluctuations during scratching for the higher current densities, which can be attributed to the rougher surface. On the one hand, when the scratch tip penetrates from the coating into the substrate, the difference of the COF of the two materials can lead to the fluctuation observed. On the other hand, the change of COF can be also a useful indicator for failure during scratching. As shown in Fig. 5c and d, the COF of the as-deposited samples fluctuates over a wider range, which can be correlated to the delamination observed on the surface (Fig. 6). In particular for the as-deposited samples produced at current densities of 5 and 7 A·dm^{-2}, the COF varied from around 0.025 to 0.175, which we attribute to the coating fragment spallation (marked by circles in Fig. 6).

Figure 6 shows the images of one scratch track on each coating examined by CLSM. The scratch direction is from left to right with increasing load, which corresponds to the gradual increase of the scratch width from left to right. The scratch width and the fracture modes were found to increase with increasing normal load. Cracks were caused by the formation of stresses in front of, beneath and behind the moving tip. In the tested FeCrNi-Al$_2$O$_3$ composite coatings, the apices of certain nodules were worn, and some nodules were even peeled off. Coating fragments and debris were pushed upwards at the banks and in front of the scratch tracks.

Two major failure modes will be discussed below, i.e., cohesive failures in the coating and adhesive failures between the coating and the steel substrate. First, concentric transverse cracks were observed within scratches in Figs. 6 and 7. Cohesive microcracks were observed on both the as-deposited and annealed samples. These cracks were curved in the direction opposite to the direction of movement of the scratch tip. These curved cracks are caused by local tensile stresses generated on the backside of the tip during dynamic contact, causing the formation and propagation of cohesive cracks.[30] In all samples, these tensile cracks become more
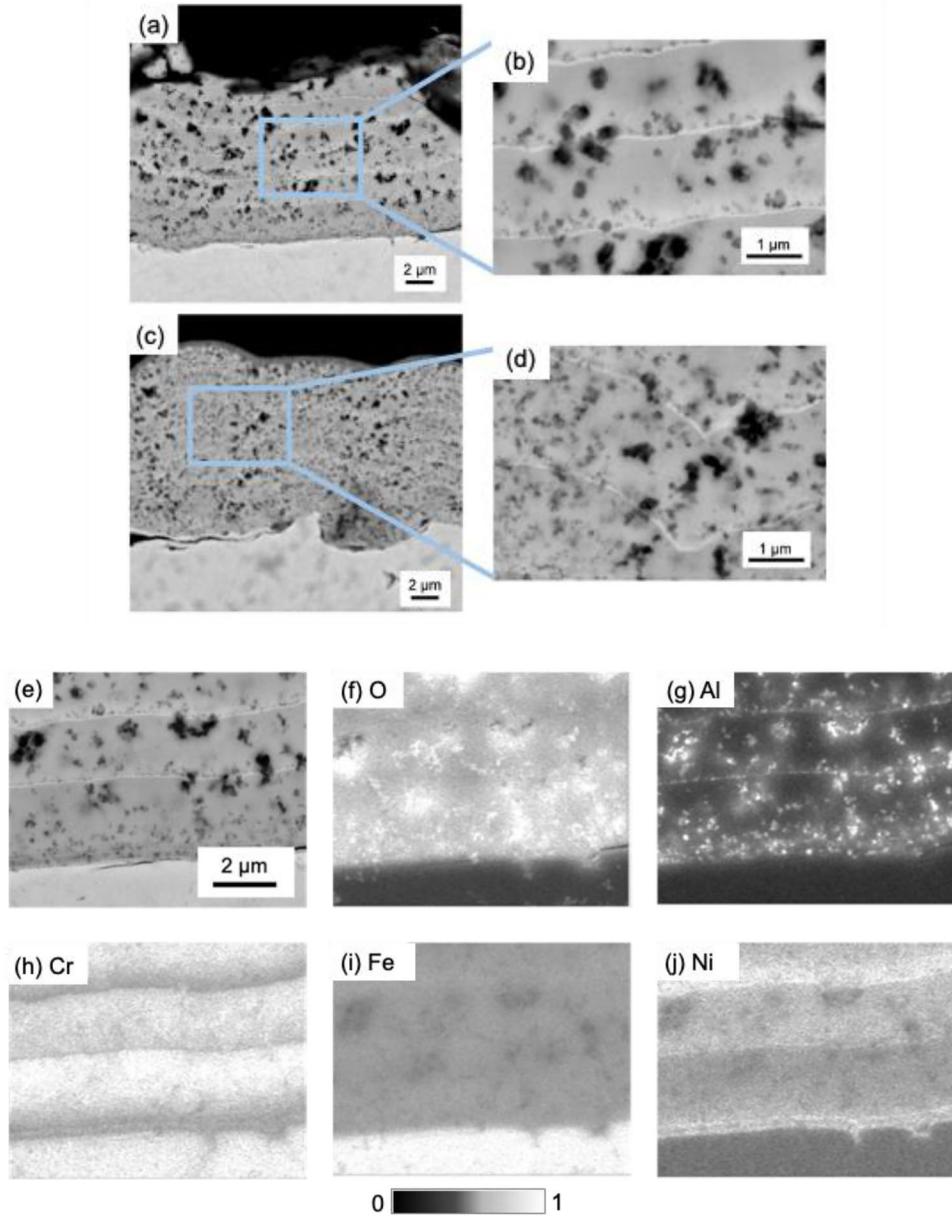
Fig. 2. SEM images of cross sections of the FeCrNi-Al_2O_3 composite coatings on a steel substrate for a current density of 5 A·dm^{-2}. (a), (b) In the as-deposited sample, most nano-sized particles were located at the bottom of the coating layers, and (c), (d) in the annealed sample, particles were distributed homogeneously in the coating layers. The element distribution from EDS: (e) SEM micrograph of the as-deposited 5 A·dm^{-2} sample cross section. The brighter regions in the images shown in (f)–(j) indicate the higher content of elements O, Al, Cr, Fe, Ni. The particles observed in (f) and (g) are Al_2O_3.

pronounced with increasing load. When the normal forces are comparatively low, the cohesive cracks mainly occupy the areas near the banks of the wear track. These cracks become more pronounced and begin to occupy the entire width of the scratch track at higher applied normal loads.

Furthermore, some of these cracks even extended beyond the scratch tracks in the 3 A·dm^{-2} samples. As marked by arrows in Fig. 7, the cracks occurred along the banks of the scratches but at an angle to the direction of indenter motion. These angled cracks are observed near the location at which the first cohesive cracks were found in the scratch track.

These angled cracks are caused by the combination of tensile stresses behind the moving tip and tensile stresses perpendicular to scratch because of the bending moment of the tip at the banks of scratch tracks.[31] At lower scratch loads, these angled cracks are finer, but they become more visible as the load continues to increase. It should be noted that according to the study of Xie et al.,[32] these angled cracks occur because of the plastic deformation of the substrate at a higher load when the coating spallation takes place. Since the steel substrate is softer than the FeCrNi-Al_2O_3 composite coating, the coating needs to bend, which induces stresses on the
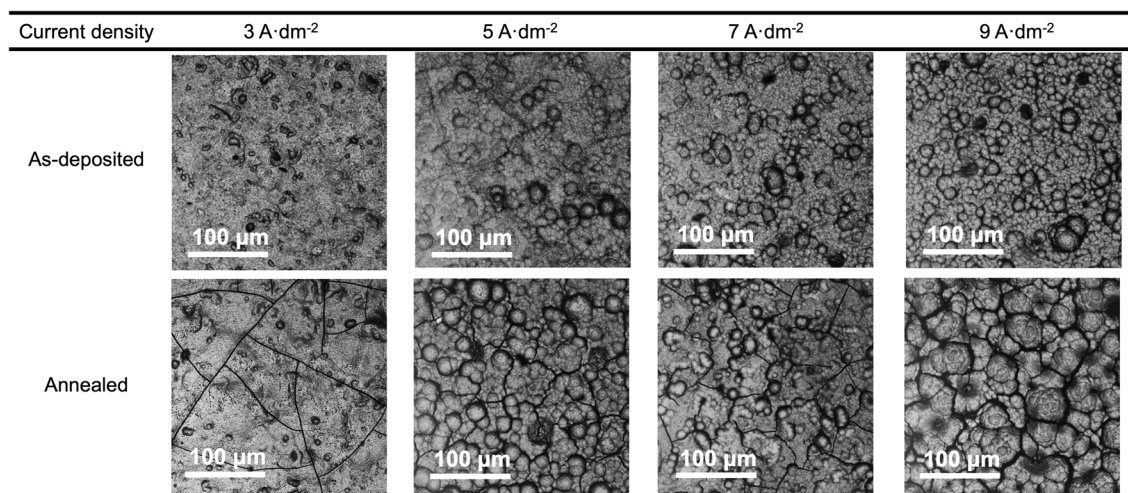
Fig. 3. The coating surfaces were investigated by confocal laser scanning microscopy in the as-deposited and annealed conditions for four deposition current densities. With increasing current density (from left to right in the panel), the roughness of the as-deposited coatings (upper row) increases. After annealing cracks were observed, the density of which—together with the surface roughness—can be seen to increase with increasing deposition rate.
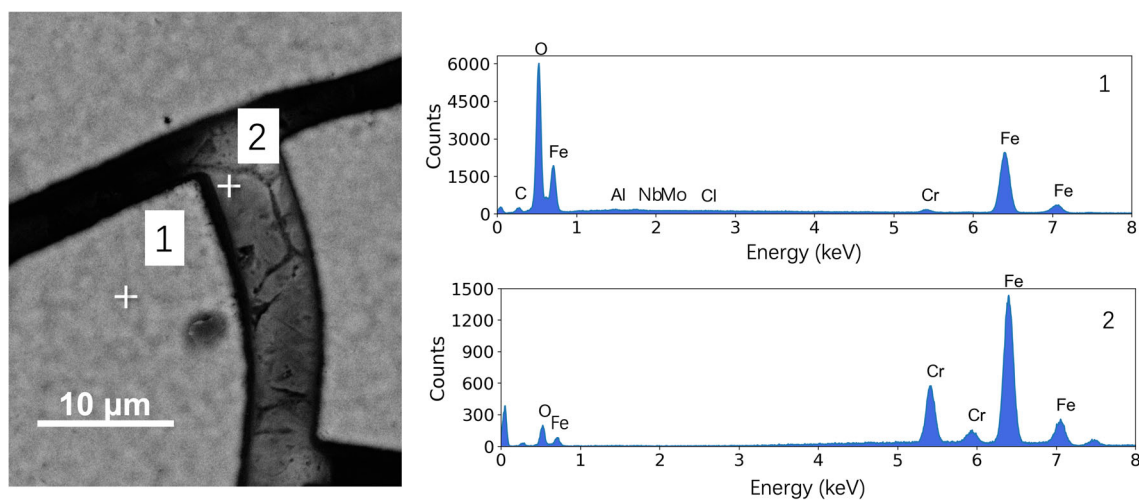

Fig. 4. SEM image (light-gray areas are the coating surface and dark areas are open cracks in the coating) with the two locations of the EDS measurements (point 1 on the surface and point 2 inside the crack) and EDS count spectra for these two locations on the surface of an annealed sample deposited at 3 A·dm^{-2}, showing a significant amount of oxygen and other main elements on the coating surface.

banks of the scratch track. Therefore, angled cracks form at the scratch banks to relieve these stresses caused by the moving tip and the bending of the coating.

In addition, adhesive failure between the coating and the substrate was observed in or adjacent to the scratch tracks, resulting in the coating spallation. In most samples, spalling resulted in the loss of small coating fragments. Plowing by the scratch tip resulted in a groove on the surface with materials being pushed to the sides. Coating delamination in a larger scale, i.e., in the form of spallation by wedging, occurred for the as-deposited samples fabricated with a current density of 5 A·dm^{-2} and 7 A·dm^{-2}. This wedging spallation can be seen (circled in Fig. 6) as bright blocks within and along

the banks of the scratch tracks, leading to the dramatic increase in scratch width and scratch depth. Two profiles, shown in Fig. 8a, were recorded perpendicular to the scratch direction, and the relative heights along the two lines were quantified from the area measurements using Gwyddion[26] (Fig. 8b). Line 1 runs through the adhesive failure region and shows a sudden height decrease, illustrating the delamination of a coating fragment. Figure 8 shows the failure of the coating and exposure of the steel substrate due to the wedging spallation by analyzing the height profile and chemical composition.

Moreover, a relatively high Mn content belongs to the steel substrate at position 3, while no Mn was detected on the coating surface at position 4
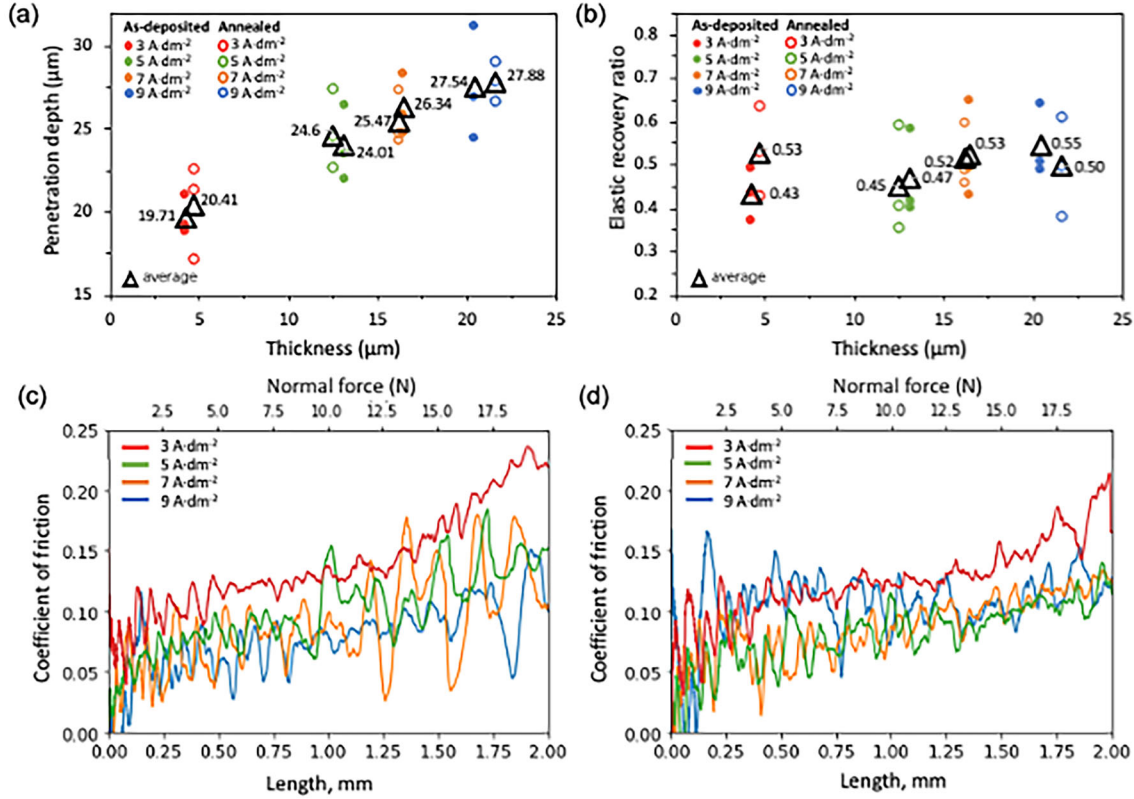
Fig. 5. (a) Maximum penetration depth of each scratch and mean values of three scratches with the same loading condition. The maximum penetration depth slightly increased with increasing coating thickness. (b) No significant variations between the different samples and coating thicknesses can be seen, as reflected in the elastic recovery ratio (ERR). The apparent COF increases with increasing normal load over the scratch length for the (c) as-deposited coatings and (d) annealed coatings.

(Fig. 8c). This EDS result indicates the exposure of substrate at the location of adhesive failure. Bull and Berasetegui[33] reported that thick coatings (typically > 10 μm) tend to show through-thickness fracture and will fail by wedge spallation. These combined stress fields, which lead to the formation of wedging fracture, arise from the residual stress after the indenter has passed the point of interest and from the bulging of the coating. It was argued that first compressive shear cracks emerge at a considerable distance in front of the indenter, traversing through the entire thickness of the coating.[22] These cracks then extend to the surface and interface, typically exhibiting sloping sides that function like a wedge. As the indenter continues to advance, it forces the coating upwards along the wedge, thereby initiating the propagation of an interfacial crack. With the progression of interfacial failure, the wedge elevates the coating further away from the substrate, introducing bending stresses within it. Sufficiently large displacements eventually lead to the detachment of the region ahead of the indenter in response to the tensile bending stresses. In the present study, wedge spallation was only observed in the as-deposited samples with the 5 A·dm^{-2} and 7 A·dm^{-2} current density. In the other samples, different failure mechanisms occurred. The thinner coating thickness of the 3 A·dm^{-2}

sample resulted in buckling, which is the most common failure mode in response to an applied stress.[33] The higher current density (9 A·dm^{-2}) and annealing were found to eliminate the severe wedging failure that leads to substrate exposure. After exposure to 500°C, the residual stresses and the development of cracks were reduced, which in turn led to a significant reduction of the delaminated area.

According to the occurrence of different types of failure, three critical forces were measured and compared for different samples. Table III lists the critical values, while the specific positions for these particular failures are marked in Fig. 6 on different scratches. Notably, a high critical force indicates that the film is more resistant to this type of failure than samples with a lower critical force. Table III shows that the critical forces of cohesive failure (L_{C1}) and discontinuous delamination (L_{C2}) decreased with increasing current density and after annealing. The samples with higher current density exhibited lower critical forces and were thus less resistant to scratching, which may be attributed to the higher stress concentrations in the rougher coatings produced by the higher current densities.[34] Cohesive cracks are present at lower normal forces in annealed samples because of a reduced deformation
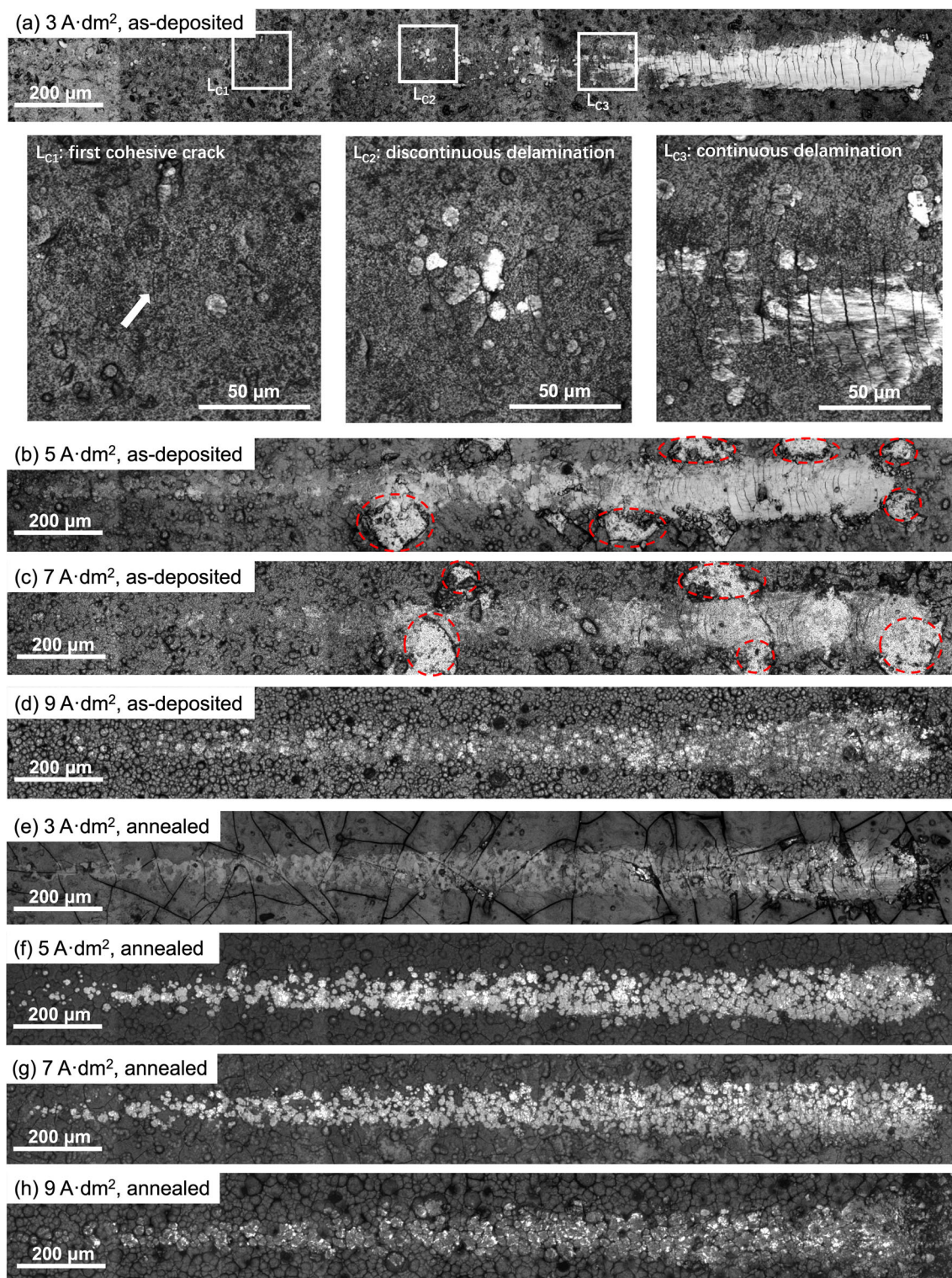
Fig. 6. Scratch tracks on the different FeCrNi-Al$_2$O$_3$ composite coatings imaged by CLSM. Cohesive and adhesive failure types can be observed. Three typical failure locations (L_{c1}, L_{c2}, L_{c3}) were identified and marked for the 3 A·dm^{-2} as-deposited sample, from which critical forces were determined.

tolerance, as noted in the study by Valentini et al.[35] The scratch tracks of the annealed samples show finer cracks than those of the as-deposited samples.

However, a higher critical force L_{C3} for continuous delamination is observed for coatings deposited at the highest current density. This observation indicates that a higher force is required to
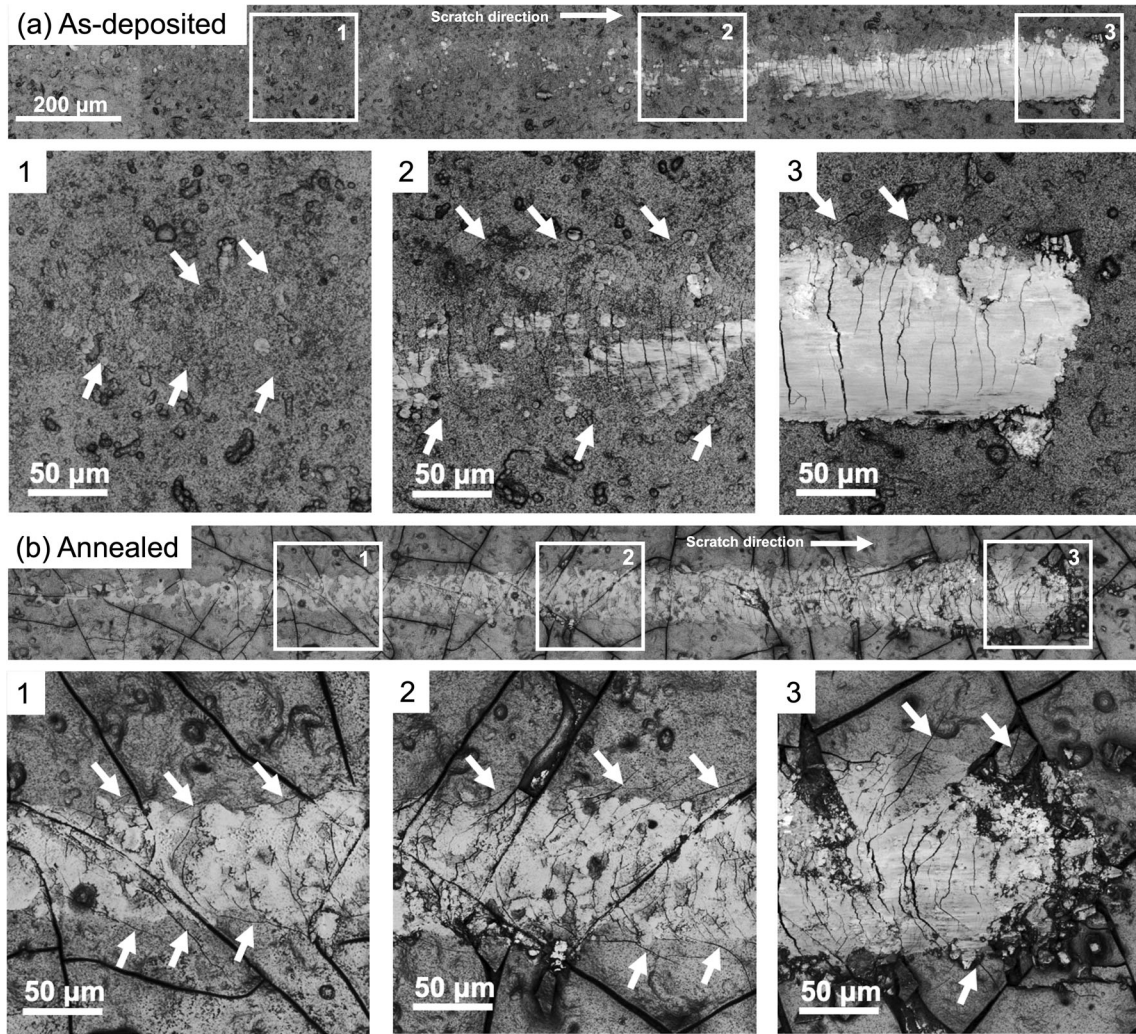
Fig. 7. CLSM images of scratch tracks on 3 A·dm^{-2} processed samples: (a) as-deposited, (b) annealed. Angled cracks (marked by white arrows) occur at the scratch banks, which became more visible with the increase of the applied load during the test.

continuously remove the coating from the substrate if the coating is thicker than if the coating is thin as for samples with a lower current density. Valentini et al.[35] argue that annealing enhances the adhesion between coating and substrate since continuous adhesive failure did not occur in the annealed samples.

Therefore, increasing the electrodeposition current density enhances the scratch resistance of the coatings and prevents the occurrence of continuous delamination at lower loads, albeit with the presence of cohesive and adhesive failures in the high current density coatings. For the annealed samples, lower critical forces for cohesive and discontinuous delamination were observed accompanied by many cracks. These cracks reduce the stresses around them and therefore protect the sample from further continuous delamination.

Indentation Behavior

The average values of Young's modulus and hardness are given in Table IV. Compared to the coated samples, the steel substrate has the highest Young's modulus and lowest hardness. The decrease of Young's modulus is attributed to the presence of amorphous phases in FeCrNi-Al$_2$O$_3$ composite coatings, which have a larger free volume fraction than crystalline phases, leading to softening of the material.[36] In addition, the cracks may also contribute to the reduction of Young's modulus measured.

The effects of the heat treatment on the mechanical properties appear more pronounced than the effects of the electrodeposition current density. After annealing at 500°C, Young's modulus and hardness increased. In general, the annealed films are oxidized and thus have a higher hardness than the metal. In addition, Al$_2$O$_3$ particles tend to be
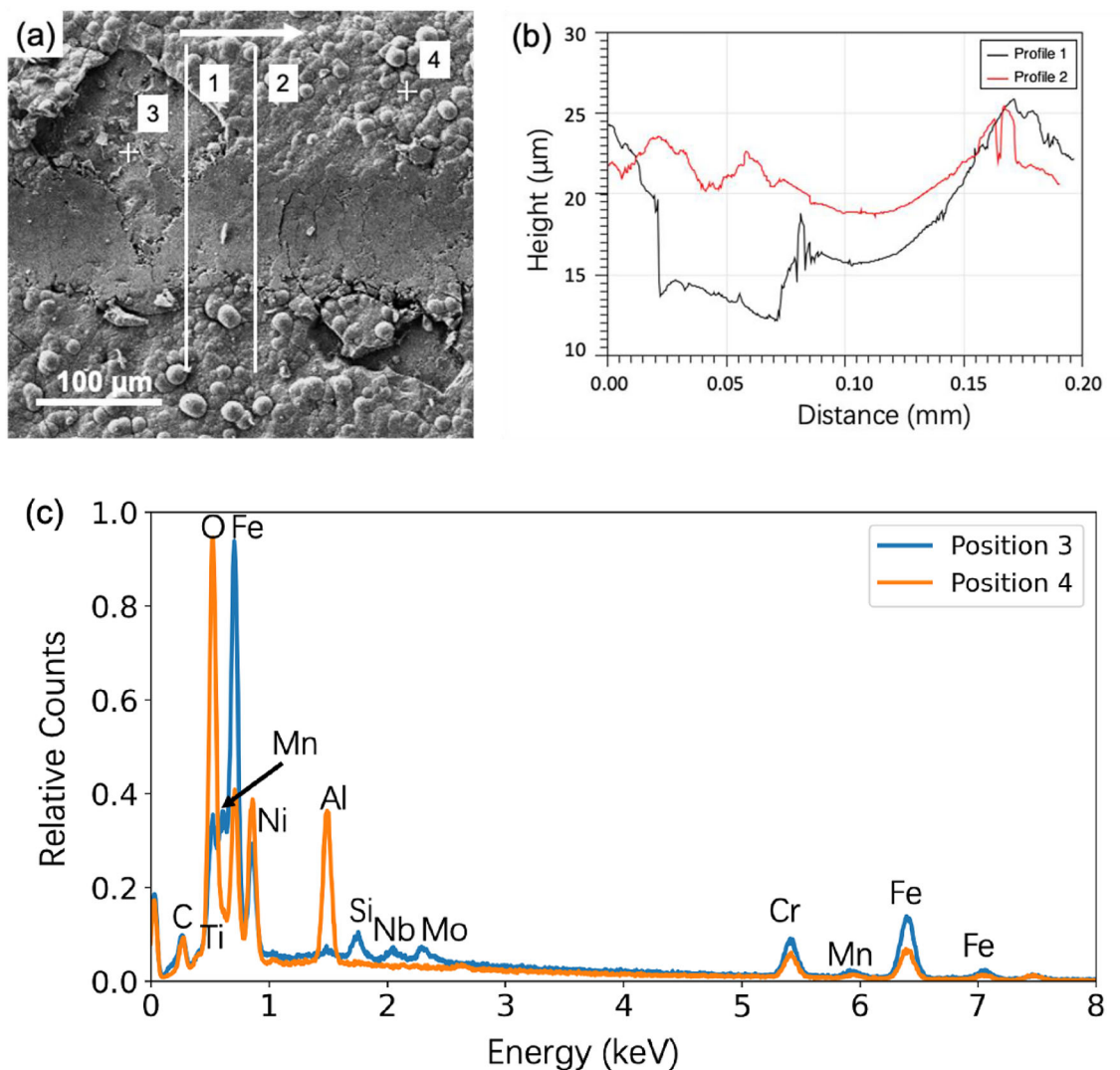
Fig. 8. (a) SEM image of adhesive failure region in the scratch track on 5 A·dm^{-2} as-deposited sample. (b) Depth profiles through the scratch track at the location of the adhesive failure region and away from it (positions 1 and 2 in (a)), indicating there was a loss of a coating fragment due to adhesive failure. (c) EDS results of two locations (indicated in (a): position 3 at the adhesive failure region and position 4 away from the scratch track). The comparison shows the occurrence of Mn at the adhesive failure region.

Table III. Critical loads determined from scratch tracks

Sample				
Current density (A·dm^{-2})	Heat treatment	L_{C1} (N)	L_{C2} (N)	L_{C3} (N)
3	As-deposited	5.15 ± 0.09	8.77 ± 0.23	13.83 ± 0.25
	Annealed	4.93 ± 0.23	14.17 ± 0.67	Not observed
5	As-deposited	6.90 ± 0.10	7.37 ± 0.38	12.70 ± 0.70
	Annealed	1.70 ± 0.36	4.13 ± 0.49	Not observed
7	As-deposited	5.55 ± 0.33	6.23 ± 0.23	15.30 ± 0.66
	Annealed	1.57 ± 0.15	3.83 ± 0.74	Not observed
9	As-deposited	3.27 ± 0.67	4.22 ± 0.12	17.48 ± 0.10
	Annealed	3.23 ± 0.29	3.57 ± 0.06	Not observed

Table IV. Average hardness (H) and Young's modulus (E) together with the respective standard deviation determined from 12 indentation tests per sample

Sample					
Current density (A·dm^{-2})	Heat treatment	Hardness H (GPa)	Young's modulus E (GPa)	H/E (*10^{-2})	H^3/E^2 (*10^{-2})
316L steel substrate		3.06 ± 0.18	187.01 ± 10.18	1.62	0.08
3	As-deposited	4.72 ± 0.23	125.82 ± 4.84	3.84	0.67
	Annealed	6.41 ± 0.34	185.38 ± 8.32	3.49	0.78
5	As-deposited	4.47 ± 0.37	91.00 ± 6.45	4.93	1.10
	Annealed	10.97 ± 0.71	175.60 ± 8.86	6.31	4.33
7	As-deposited	4.61 ± 0.19	97.27 ± 4.79	4.72	1.02
	Annealed	8.42 ± 0.95	151.87 ± 9.99	5.48	2.61
9	As-deposited	5.56 ± 0.32	98.04 ± 4.48	5.69	1.83
	Annealed	7.46 ± 0.98	121.52 ± 7.66	6.13	2.94

distributed more homogeneously after annealing, which is also related to the hardness improvement. Except for the 3 A·dm^{-2} sample, Young's modulus of the as-deposited samples did not change much for different current densities. The relatively higher Young's modulus of the 3 A·dm^{-2} as-deposited sample is related to the absence of pores and cracks, which would reduce both stiffness and Young's modulus. Increasing current density and annealing are beneficial to the hardness of the coating. This higher hardness and the increased coating thickness at higher current densities are the reasons for the increase of the critical force for continuous delamination L$_{C3}$ (Table III), which occurred for samples deposited by current densities from 5 A·dm^{-2} to 9 A·dm^{-2} as discussed in "Scratch behavior" section. The annealed samples did not exhibit continuous adhesive failures, and the absence of this failure type is attributed to the increased hardness of the annealed samples.

Hence, the increase of current density from 5 A·dm^{-2} to 9 A·dm^{-2} slightly improves the hardness from 4.47 ± 0.37 GPa to 5.56 ± 0.32 GPa in the as-deposited samples, as listed in Table IV. In general, the improvement of hardness can be achieved by microstructure refinement and chemical composition adjustment. It has been reported that increased current density can result in a higher nucleation rate than grain growth rate, thereby resulting in a smaller average grain size in the Fe-Cr-Ni alloy deposits.[37] However, the effects of current density on microstructure refinement, i.e., the grain size, in the metal matrix have not been quantified. In addition, we assume that the enhanced hardness is related to the higher Cr content in the metal matrix at higher current density, since Cr is harder than Fe and Ni, which are soft magnetic materials with lower hardness. However, increasing current density resulted in the opposite effect on hardness of the annealed samples. After the heat treatment, while the hardness is greatly enhanced compared to the as-deposited samples, a decreasing trend in hardness of samples with current density from 5 A·dm^{-2} to 9 A·dm^{-2} can be seen (Table III).

Improved wear properties are associated with an increase in the hardness of a material.[38] However, the wear properties of a coating cannot be characterized by only the hardness as also the elastic behavior, surface roughness, and fracture propensity play important roles. On the one hand, a low Young's modulus value of the substrate is desirable as it allows the load to be distributed over a wider area.[38] On the other hand, stiff and brittle coatings on compliant substrates lead to bending stresses in the coating during indentation and scratch experiments and may cause crack formation in the coating or delamination of the coating.[39] In this study, the highest H/E and H^3/E^2 ratios were observed for the annealed sample deposited at 5 A·dm^{-2}, which have the highest hardness among all tested samples and a relatively low Young's modulus compared to the other samples. Thus, this sample should have the best wear resistance when applying the criteria based on the indentation results. However, the critical force evaluation that relies on the scratch experiments gives a more detailed picture, as discussed in "Depth-sensing indentation" section.

CONCLUSION

FeCrNi-Al$_2$O$_3$ composite coatings on 316L steel substrates were fabricated by electrodeposition with current densities ranging from 3 A·dm^{-2} to 9 A·dm^{-2}. Some samples were then annealed at 500°C in Ar atmosphere. In this study, scratch and nanoindentation experiments were conducted to study the effects of the current density and the

annealing on the micromechanical properties of these metal-ceramic thin films. The main conclusions drawn from this study are summarized below:

1. By increasing the current density, the thickness of as-deposited coatings increases as a result of the increased deposition and growth rate. Annealing does not have a significant influence on the coating thickness. The roughness further increased during annealing, showing bigger nodules and denser micro-cracks on the coating surface.

2. During the scratch test, the tip penetrated deeper into the coating as the coating thickness increased. However, the elastic recovery ratio did not significantly change when the current density and heat treatment changed.

3. Cohesive cracks and adhesive spallation are inevitable in scratch tracks. No catastrophic wedging delamination and continuous substrate exposure appeared in the annealed samples, indicating that annealing improves the adhesion between coating and substrate and results in residual stress relief. Alternatively, it can be argued that the high propensity to cohesive failure results in sufficient stress relief in annealed coatings so that the stresses never reach the delamination strength.

4. The higher current density reduces or even eliminates angled cracks. A correlation is found between the improved scratch performance and the hardness increase as well as its H/E and H^3/E^2 ratios.

5. The coating/substrate system has a higher hardness than the pure steel substrate. The hardness of the as-deposited coatings was slightly improved by increasing the current density and largely enhanced by thermal treatment. However, the higher current density does not increase the hardness of the annealed samples.

FUNDING

CONFLICT OF INTEREST

All authors declare that they have no conflicts of interest.

OPEN ACCESS

REFERENCES

1. P. Kumar, R. Kumar, V. Rai, and A. Manash, *IRJASH* 4, 318 (2022).
2. F. Presuel-Moreno, M.A. Jakab, N. Tailleart, M. Goldman, and J.R. Scully, *Mater. Today* 11, 14 (2008).
3. M. Sathish, N. Radhika, and B. Saleh, *Compos. B Eng.* 225, 109278 (2021).
4. F.C. Walsh, S. Wang, and N. Zhou, *Curr. Opin. Electrochem.* 20, 8 (2020).
5. V. Torabinejad, M. Aliofkhazraei, S. Assareh, M.H. Allahyarzadeh, and A.S. Rouhaghdam, *J. Alloy. Compd.* 691, 841 (2017).
6. M. Alizadeh and H. Safaei, *Appl. Surf. Sci.* 456, 195 (2018).
7. G. Figueira, C.A.D. Rovere, and P. Gargarella, *J. Market. Res.* 13, 2527 (2021).
8. A. Bai, C.-C. Hu, and T.-C. Wen, *Electrochim. Acta* 48, 2425 (2003).
9. L. Xu, J. Du, S. Ge, N. He, and S. Li, *J. Appl. Electrochem.* 39, 713 (2009).
10. M. Tavoosi and A. Barahimi, *Surf. Interfaces* 8, 103 (2017).
11. E. Bertero, M. Hasegawa, S. Staubli, E. Pellicer, I.K. Herrmann, J. Sort, J. Michler, and L. Philippe, *Surf. Coat. Technol.* 349, 745 (2018).
12. E. Bertero, C.V. Manzano, E. Pellicer, J. Sort, R.M. Ulfig, S. Mischler, J. Michler, and L. Philippe, *RSC Adv.* 9, 25762 (2019).
13. M. Winnicki, *Coatings* 11, 1044 (2021).
14. B.S. Vasile, A.C. Birca, V.A. Surdu, I.A. Neacsu, and A.I. Nicoară, *Nanomaterials* 10, 370 (2020).
15. M.R. Vaezi, S.K. Sadrnezhaad, and L. Nikzad, *Colloids Surf. A* 315, 176 (2008).
16. N.S. Mbugua, M. Kang, Y. Zhang, N.J. Ndiithi, G.V. Bertrand, and L. Yao, *Materials* 13, 3475 (2020).
17. L. Benea, P. Ponthiaux, and F. Wenger, *Surf. Coat. Technol.* 205, 5379 (2011).
18. B. Nikravesh, B. Ramezanzadeh, A.A. Sarabi, and S.M. Kasiriha, *Corros. Sci.* 53, 1592 (2011).
19. R. Starosta and A. Zielinski, *J. Mater. Process. Technol.* 157–158, 434 (2004).
20. L.M. Chang, J.H. Liu, and R.J. Zhang, *Mater. Corros.* 62, 920 (2011).
21. X. Luo, Z. Yao, P. Zhang, and D. Gu, *J. Alloy. Compd.* 755, 41 (2018).
22. Z. Feng, M. Tang, Y. Liu, Z. Yan, G. Li, and R. Zhang, *Surf. Eng.* 34, 309 (2018).
23. S. Lafaye, C. Gauthier, and R. Schirrer, *Wear* 265, 664 (2008).
24. J. Liu, Q. Zeng, and S. Xu, *Constr. Build. Mater.* 254, 119255 (2020).
25. X. Li and B. Bhushan, *Mater Charact* 48, 11 (2002).
26. D. Nečas and P. Klapetek, *Open Phys.* 10, 181 (2012).
27. N.P. Wasekar, P. Haridoss, S.K. Seshadri, and G. Sundararajan, *Surf. Coat. Technol.* 291, 130 (2016).
28. L. Zhu, S. Bai, H. Zhang, and Y. Ye, *Appl. Surf. Sci.* 265, 537 (2013).
29. V. Nemane and S. Chatterjee, *Mater Charact* 180, 111414 (2021).
30. S.J. Bull, *Surf. Coat. Technol.* 50, 25 (1991).
31. A. Ghabchi, S. Sampath, K. Holmberg, and T. Varis, *Wear* 313, 97 (2014).

32. Y. Xie and H.M. Hawthorne, *Surf. Coat. Technol.* 155, 121 (2002).
33. S.J. Bull and E.G. Berasetegui, *Tribol. Int.* 39, 99 (2006).
34. B. Feng, *AIP Adv.* 7, 035217 (2017).
35. R. Valentini, P. Cavaliere, and D. Valerini, *Tribol. Mater. Surf. Interfaces* 14, 22 (2020).
36. J.T. Kim, S.H. Hong, C.H. Lee, J.M. Park, T.W. Kim, W.H. Lee, H.I. Yim, and K.B. Kim, *J. Alloy. Compd.* 587, 415 (2014).
37. E. Yousefi, A. Irannejad, and S. Sharafi, *Trans. Nonferrous Metals Soc. China* 29, 2591 (2019).
38. J. Musil, F. Kunc, H. Zeman, and H. Polakova, *Surf. Coat. Technol.* 10, 304 (2002).
39. Q. Wang, F. Zhou, M. Callisti, T. Polcar, J. Kong, and J. Yan, *J. Alloy. Compd.* 708, 1103 (2017).